Fuel 248 (2019) 16–26

Contents lists available at ScienceDirect

Fuel

journal homepage: www.elsevier.com/locate/fuel

Full Length Article

Influence of ethanol blending ratios on in-flame soot particle structures in an optical spark-ignition direct-injection engine

Yi Gao[a], Dongchan Kim[b], YiLong Zhang[b], Sanghoon Kook[b,*], Min Xu[a]

[a] Department of Mechanical Engineering, Shanghai Jiao Tong University, Shanghai, China
[b] School of Mechanical and Manufacturing Engineering, The University of New South Wales, Sydney, Australia

ARTICLE INFO

Keywords:
Ethanol
Petrol
Soot particles
Direct injection

ABSTRACT

This study shows how ethanol addition impacts in-flame and exhaust soot in spark-ignition direct injection (SIDI) engines through direct and simultaneous sampling of particles from the flames and exhaust stream. The thermophoresis-based soot sampling and transmission electron microscope (TEM) imaging was performed for various ethanol blending ratios ranging from 0 to 60%. A quantitative analysis is performed in the images obtained from a standard TEM by yielding the in-flame and exhaust soot number counts, projection area, as well as morphological parameters such as soot primary particle diameter, aggregate radius of gyration, and fractal dimension. In addition, the internal structures and reactivity status of in-flame and exhaust soot particles are unveiled using a high-resolution TEM with carbon fringe length, tortuosity and fringe-to-fringe separation extracted from processed carbon layer fringe images. The results show that both the number counts and projection areas of exhaust soot are much lower than those of the in-flame soot at any fixed ethanol blending ratios. The exhaust soot is smaller in size for both the primary particles and aggregates with more compact aggregate structures, longer and straighter fringe, and lower fringe separation, all indicating significant soot oxidation occurred inside the cylinder before the particles exit through the exhaust. With increasing ethanol blending ratio, almost linear reduction in number counts and projection area is found for both the in-flame and exhaust soot particles, while both soot aggregates and primary particles become smaller with more stretched aggregate structures and shorter, more curved, and narrower gap fringe structures, indicating soot particles with higher reactivity. The significantly lower soot emissions achieved with higher ethanol blending ratio is found to be due primarily to the suppression of soot formation within the flame as evidenced by higher reduction rate of number counts, projection area, and primary particle and aggregate sizes for the in-flame soot than that of the exhaust soot.

1. Introduction

Spark-ignition direct-injection (SIDI) engines have become one of the mainstream technologies in the automotive industry thanks to fuel economy benefits over port-injection engines. However, SIDI engines were found to produce large amounts of particulates [1] such as soot particles [2], which were traditionally problematic only in diesel engines. This raised serious environmental and health concerns, which led to the introduction of emission regulations on both the particulate number (PN) and particulate mass (PM) [3]. Liaising particulate filter technology used for diesel engines, one immediate solution to PN/PM emissions is a gasoline particle filter (GPF) [4]. However, the increased cost is unavoidable making already costly direct-injection engines less attractive [5]. Also, the GPF efficacy is high only when particulates are small enough to be caught by Brownian motion or sufficiently large to be captured by porous barriers, leaving efficacy pithole in a certain size range (e.g. 50 nm–200 nm in diameter) [4]. Another solution is a higher pressure injection system (e.g. 40 MPa [6,7]), which is expected to enhance air/fuel mixing and thereby significantly reducing in-cylinder soot formation from locally rich mixtures [6]. However, a similar cost issue exists for higher pressure injection systems.

An alternative approach could be the use of ethanol. In addition to the advantages of reduced use of petroleum and lower CO_2 emissions [8,9], an oxygenated ethanol was previously shown to produce significantly lower amounts of particulate emissions in diesel engines [10]. Given ethanol has successfully penetrated into the market in a form of ethanol blends in petrol [8,11], it is also a practical option for SIDI engines. In this regard, there is a clear need for enhanced fundamental

* Corresponding author.
E-mail address: s.kook@unsw.edu.au (S. Kook).

https://doi.org/10.1016/j.fuel.2019.02.131
Received 27 November 2018; Received in revised form 21 February 2019; Accepted 26 February 2019
Available online 16 March 2019
0016-2361/ © 2019 Elsevier Ltd. All rights reserved.

understanding of soot formation process occurring in ethanol fuelled SIDI engines, to which the present study makes a unique contribution.

Previous studies reported the positive effect of ethanol on particulate emissions from the engine tests performed for various ethanol blending ratios of E10–E85 (i.e. 10–85% ethanol blended in petrol) with an emphasis on PM [12–17] and PN reduction [13,17–19]. For example, it was shown that even low ethanol blends such as E10 can lead to a statically significant reduction in PM/PN emissions compared to petrol [17]. When a higher blending ratio (e.g. E85) was used, the PM emissions remained very low even for extremely advanced fuel injection timings at which the sooting level of petrol fuel measured by the filtered smoke number increased significantly [13]. The observed trends were expected as both lower soot formation rate and higher oxidation rate of the oxygenated fuels [20,21] would result in reduced engine-out particulate emissions.

However, there are other studies reporting negligible or even negative effects of ethanol on PM [14,18,22–27] and PN [14–16,22–25,28,29] emissions, especially if a low blending ratio of 20% or lower is used [14,15,22,30–34]. One of these studies [22] also showed increased soot luminosity signals inside the cylinder. One possible cause for the increased PM emissions was poor evaporation, which led to locally rich mixtures and thereby increasing soot formation [18,20,22,27,28]. For instance, when a cold-start condition was used for engine tests, increased soot emissions were measured for E10 compared to petrol whereas a warmed-up condition showed decreased soot emissions [17]. Also, the ethanol effects on soot emissions are strongly dependent upon spark timing and equivalence ratio. For example, the trends were reversed depending on the spark timing such that the retarded spark timing showed increased soot luminosity signals for E85 than that of petrol but the advanced spark timing exhibited lower soot luminosity than lower ethanol blending ratio fuels [26]. Regarding the equivalence ratio, a stoichiometric charge showed no soot reduction due to ethanol addition whereas overall rich charge conditions led to decreased soot emissions for E20 [33].

The present study aims to enhance fundamental knowledge about soot particles formed inside the cylinder of an SIDI engine so that mixed conclusions and complex trends about the influence of ethanol on in-cylinder/in-flame soot formation could be better explained. Despite the fact that soot particles are aggregates with complex fractal structures, there are limited studies about soot morphology. Previous studies conducted for exhaust soot reported minor variations of soot aggregate structures between petrol and E20 [35] but more amorphous internal soot structures for ethanol blends due to oxygenated fuel [35,36]. The present study performs both in-flame soot and engine-out soot sampling for various ethanol blends. Detailed particles structure analysis based on thermophoretic sampling of pool fire induced soot on the piston top is compared to that of engine-out soot particulates. A carbon-coated transmission electron microscope (TEM) grid and a standard-resolution TEM are used to understand the overall soot structures based on the statistical analysis of soot primary particle diameter, soot aggregate radius of gyration, and fractal dimension, similar to our previous work on diesel soot [35,37–40]. Moreover, a lacy TEM grid and a high-resolution TEM are used to process sub-nanoscale carbon layer fringes of soot particles based on the analysis of fringe length, tortuosity and fringe-to-fringe separation distance [39–44]. The complete dataset is expected to explain the soot formation and oxidation processes that occur within the flames inside the cylinder of the engine, and how they affect the engine-out soot for various ethanol-in-petrol blending ratios.

2. Experiments

2.1. Engine specification and operating conditions

The experiments were conducted in an optically accessible single-cylinder SIDI engine with a side-mounted injector, as illustrated in Fig. 1 [45–48]. The specification and operating conditions of this engine are summarised in Table 1. The displacement volume of the engine is 500 cm^3 with a square combustion chamber of 86-mm bore and stroke. For better optical access, a flat-top piston design was applied with a geometric compression ratio of 10.5. A warmed-up engine condition was used to realise thermally stable conditions by circulating heated water at 363 K through the engine head, engine block and cylinder liner. The intake air was naturally aspirated at a wide-open throttle condition with the temperature being measured at 303 K with only ± 1 K variations. The engine was driven using an induction motor to operate at a constant speed of 1200 resolutions per minute (rpm).

All the tested fuels were directly injected using a side-mounted 6-hole injector (Continental DI XL2) that was controlled with a universal signal controller (Zenobalti ZB-9013P). The injection pressure and timing were set to 15 MPa and 320 °CA bTDC, respectively, to create the high wall-wetting conditions with intended fuel-film formation on the piston top surface and thus high soot formation, as shown in our previous studies [46,47]. With increasing ethanol blending ratios, the injection duration/mass was increased, which was to keep the stoichiometric charge condition. The spark timing was varied in the 16–18 °CA bTDC range to hold the combustion phasing constant. As will be shown later, this approach resulted in almost identical in-cylinder pressure traces, meaning the same engine performance for all the soot sampling engine runs. The in-cylinder pressure was recorded using a piezoelectric pressure transducer (Optrand C822J6-SP). With the recorded pressure traces, the apparent heat release rate was also calculated.

The optical access into the combustion chamber was made through a 35-mm-tall quartz liner. The soot luminosity signals were recorded at a frame rate of 10 kHz (i.e. 0.72 °CA/frame) using a high-speed CMOS camera (VisionResearch Phantom v7.3) equipped with a 105-mm lens (Nikon Nikkor), which provides critical information about the development of sooting petrol/ethanol flames with respect to the soot sampling locations.

2.2. Fuel properties

A conventional petrol fuel with 95 research octane number (RON) and neat ethanol were used to formulate ethanol blends of E0, E10, E35 and E60. The chemical and physical properties of the petrol and ethanol used in this study are summarised in Table 2. E10 was selected due to its popularity in the market and thus availability of soot information in the literature. The ethanol blending ratio was then increased by 25% in volume up to 60% at which no engine-out soot particles were sampled.

2.3. Soot particle sampling

Depicted in Fig. 1 is the in-flame soot sampling system where a probe is installed 1 mm above the piston top and on the opposite side of the injector. This sampling location was selected based on our previous study [48], which conducted the same soot sampling experiments on various piston-top locations. As the selected location was directly opposite to the injector, the wetting-induced pool fire was found the most significant and lasting for a longer period of time than other locations. Therefore, this is a representative in-cylinder location for soot sampling. At the probe tip, a 3-mm diameter TEM grid was placed, which is protected from excessive heat using a cap. However, the cap has a small 2.7-mm hole to have the TEM grid directly exposed to the flames. This restrictive opening on the sampling probe cap was carefully designed to retain the high temperature gradient between the sooting flame and the TEM grid surface for thermophoresis-based soot deposition and rapid reaction quenching [48]. The soot-laden gases inside the cylinder were then expelled to exhaust pipe, where another sampling probe was placed in parallel to the exhaust flow. This realised the simultaneous sampling of in-flame and exhaust soot particles, similar to our previous diesel soot studies [38,48]. This was possible because the raw exhaust gas was sufficiently diluted due to the use of skip firing modes. For soot sampling experiment, the fuel injection was executed every 10th

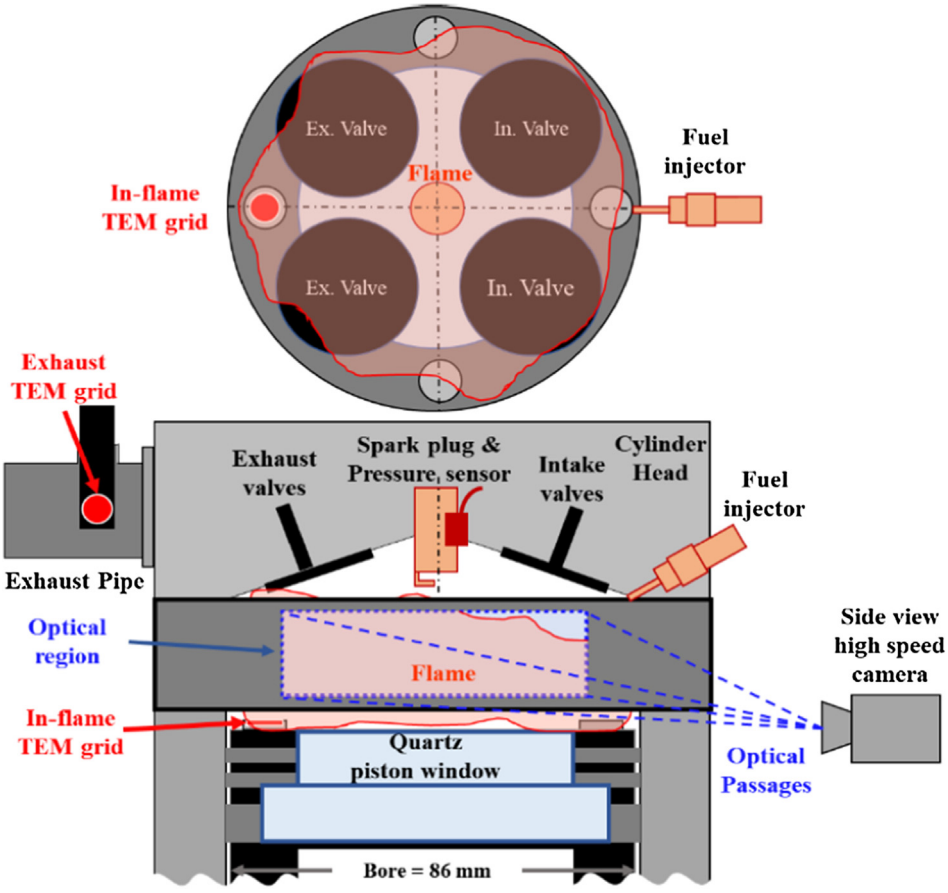

Fig. 1. Illustration of the optical SIDI engine and soot particle sampling system.

Table 1
Engine specification and operating conditions.

Displacement	500 cm^3
Bore/Stroke	86/86 mm
Compression Ratio	10.5
Valvetrain	DOHC, 4 valves
Intake Valve Timing	353–113 °CA bTDC
Exhaust Valve Timing	136–360 °CA bTDC
Engine Speed	1200 RPM
Intake Pressure	100 kPa (absolute)
Intake Temperature	303 K
Coolant Temperature	363 K
Fuel-Injection Strategy	Single injection
Fuel Pressure	15 MPa
Fuel Injector	Continental DI XL2 (6-hole, side mounted)
Injection Duration	2.40–3.08 ms
Equivalence Ratio	1
Injection Timing	320 °CA bTDC
Spark Timing	16–18 °CA bTDC
Firing Mode	10-skip firing
Number of Firing Cycles	5
Sampling Location	1 (in-flame) + 1 (exhaust)
Sampling Grid	Standard and lacy
Tested Fuel	E0, E10, E35, E60

motoring cycle (i.e. 1 firing cycle and 9 motoring cycles). This is a widely used approach in optical engines for low thermal loading on quartz windows and minimal residual gases from the previous firing cycle. Prior to the fuel injection, the engine was motored for 90 s until the in-cylinder gases reached thermally stable conditions. For each sampling run, a total of 5 injections were executed (i.e. 5 firing cycles), which was optimised in our previous study [48] considering the collection of many soot particles for statistically meaningful data analysis and the potential issue of soot overloading.

Table 2
Properties of petrol and ethanol.

Properties	Petrol [49]	Ethanol [22]
Formula	–	C_2H_5OH
Research Octane Number	95	107
Density @ 15 °C (g/cm^3)	0.73	0.793
Stoichiometric Air Fuel Ratio	14.7	9.0
Lower heat value (MJ/kg) [22]	43.5	26.8
Boiling point (°C)	35–210	78.5
Kinematic viscosity (mm^2/s) [6]	0.494	1.221
Oxygen (wt%)	0	34.7

The present study applied two types of TEM grids for soot sampling. One was a copper grid of 400 meshes with a 50-nm thick carbon film coating (standard TEM grid) for measuring the size of soot primary particles and aggregates, structural compactness of soot aggregates, as well as soot number counts and projection area. The other grid was a copper grid of 300 meshes with a 150-nm thick lacy carbon film coating (lacy TEM grid). This was used to sample soot particles on the carbon layer branches and visualise the extruded portion of the soot aggregates with no background interference from the carbon coating, which was required for the high-resolution sub-nanoscale imaging of carbon layer fringes [40].

2.4. Standard TEM imaging and post-processing

The standard TEM grids with deposited soot particles were examined under a magnification of 100,000 times in a TEM (JEOL 1400) with a 120-kV electron accelerating voltage setting and 0.38-nm point resolution. With a CCD camera, the sampled soot particles were digitised in the TEM at a pixel resolution of 1350 by 1040, leading to a fine

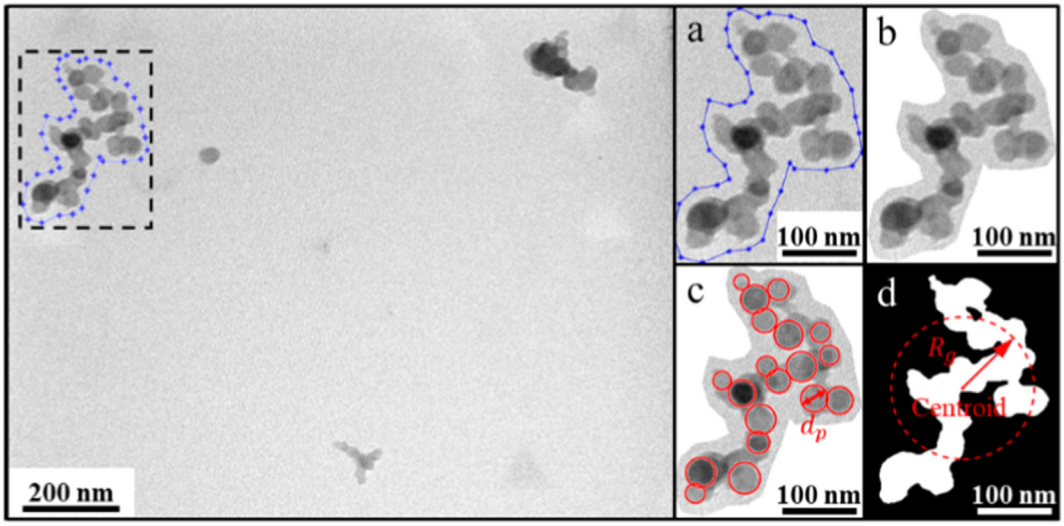

Fig. 2. TEM image post-processing procedure for soot aggregates: (a) selection of a soot aggregate; (b) selected region for processing; (c) automated detection of soot primary particles; (d) binarisation of the soot aggregate region for the projection area and radius of gyration estimation.

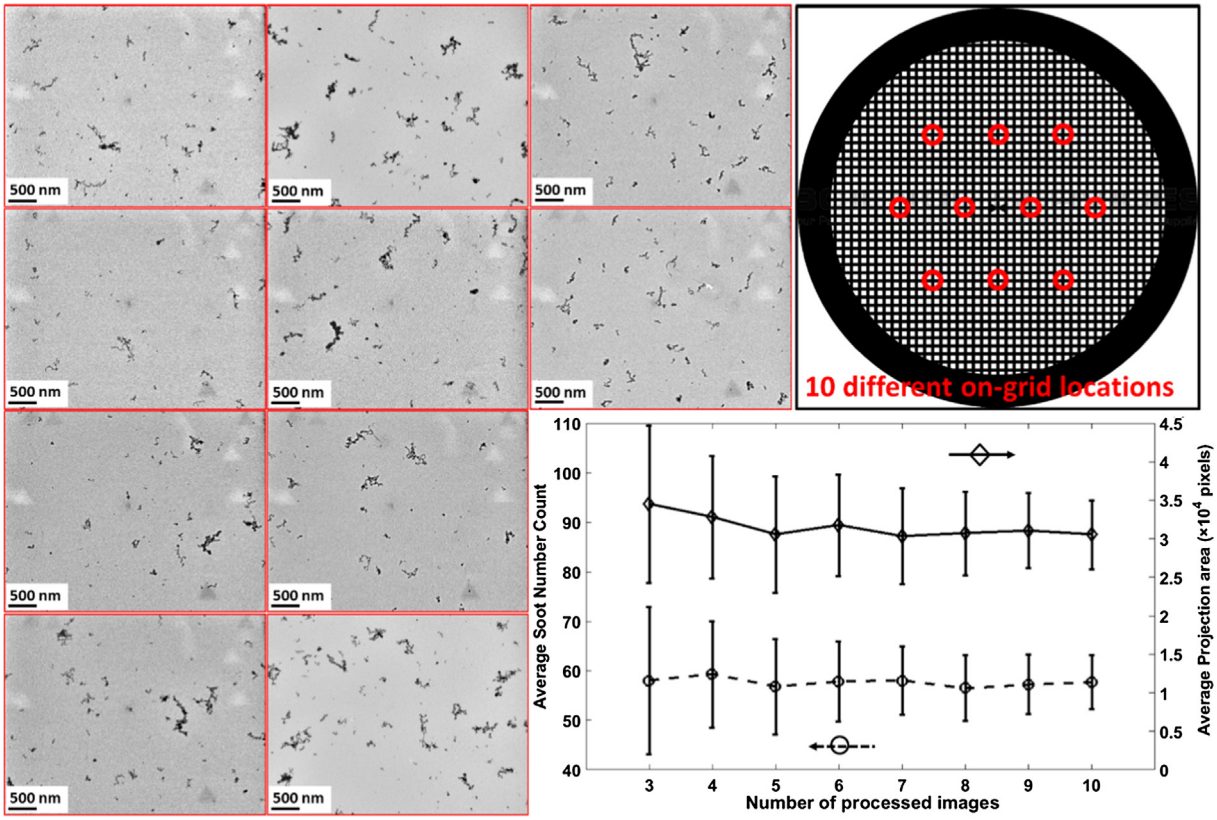

Fig. 3. Ten 30k images of E10 in-flame soot particles on standard grids. The 500-nm scale bar is shown on each image. Shown on the top-right corner is illustration of 10 different on-grid locations. The plot on the bottom-right corner shows the mean value with 95% confidence error margin for the average soot number count and projection area.

resolution of 1 nm/pixel [48]. An in-house-developed Matlab code was used to automatically post-processing the standard TEM images for the measurement of the soot primary particle diameter, aggregate radius of gyration, and fractal dimension. An example of this image post-processing is shown in Fig. 2 [50]. The standard TEM images with high quality were subject to self-subtraction and unsharp filtering for particle edge enhancement, followed by the Canny Edge Detection and Circular Hough Transform to detect circular objects (i.e. soot primary particles) within the regions of the selected soot aggregates, which then was used to measure the diameter of soot primary particles (d_p). The soot aggregates are binarised to calculate the projection area and the radius of gyration of soot aggregates (R_g). The obtained d_p and R_g were also used to determine the soot aggregate fractal dimension (D_f) [38,39]. For each TEM grid, a total of 30 on-grid locations were imaged to resolve potential spatial variation issues and to process more than 100 soot aggregates and 1000 primary particles.

In addition to the 1 nm/pixel setting, a lower resolution image of 30,000 magnification and 3.4 nm/pixel was also obtained, as shown in

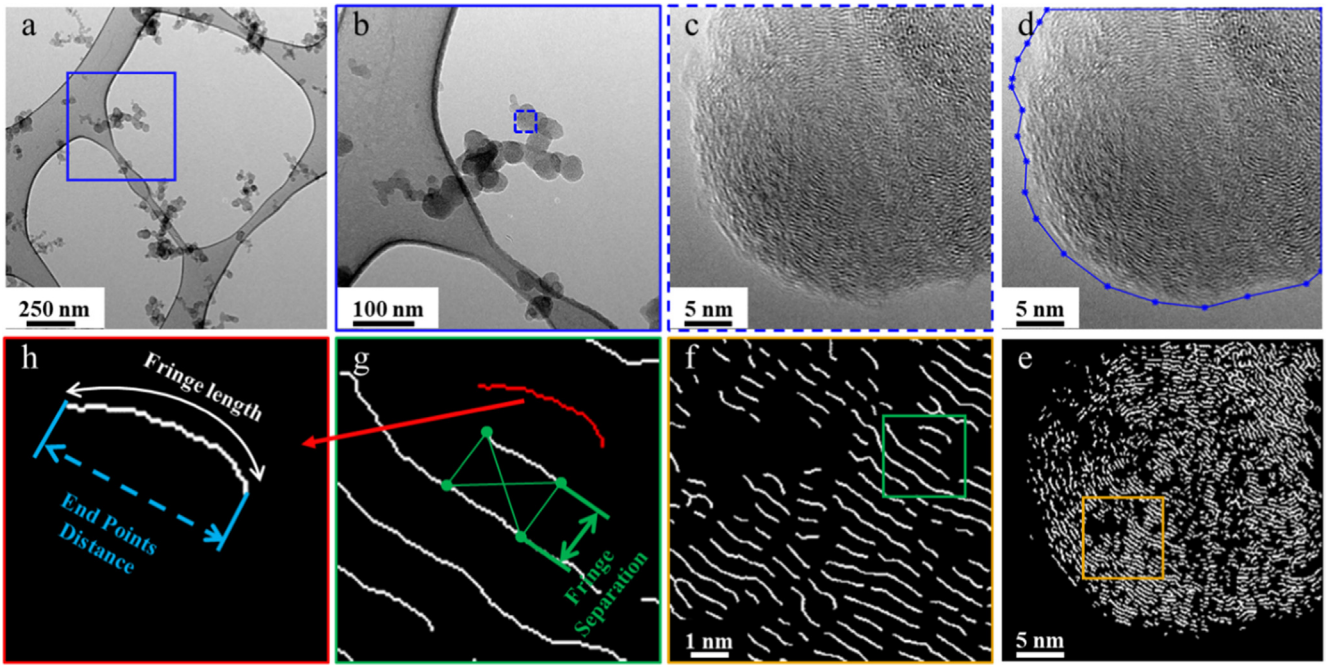

Fig. 4. Post-processing of high-resolution TEM images: (a) scanning the lacy TEM grid; (b) locating a jutting-out soot aggregate; (c) obtaining a high-resolution TEM image for selected primary particle; (d) identifying region of interest; (e) extraction of fringe skeletons; (f) a close-up view of the fringe skeletons; (g) fringe separation measurement; (h) fringe length and straight distance between the fringe endpoints.

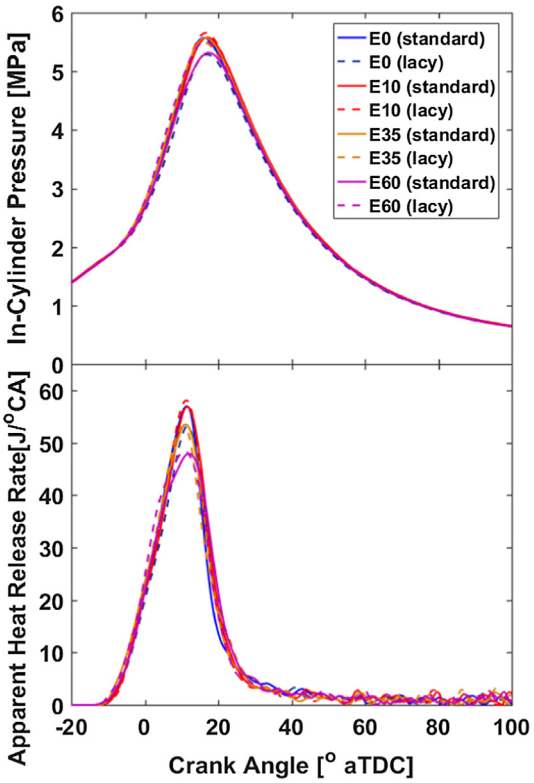

Fig. 5. Averaged in-cylinder pressure and corresponding apparent heat release rate traces for all soot sampling runs of the present study.

Fig. 3. These images were used specifically for the counting of soot aggregate/particle number and the estimation of soot amount due to their large sample volume. Fig. 3 shows 10 different TEM images and corresponding on-grid locations. It is clearly seen that the number and overall amount of the sampled soot aggregates vary on-grid location by location; however, the average soot number count and projection area plot shown on the bottom-right corner indicates that the variations (error bar for 95% confidence) decrease with increasing number of processed TEM images, and as more than 9 TEM images were processed, both the average number count and projection area do not vary much. Based on the result, a total of 10 TEM images were processed for each sample.

2.5. High-resolution TEM imaging and post-processing

The inspection of soot internal structure was performed by placing a lacy TEM grid into a high-resolution TEM (Phillips CM200) with an accelerating voltage of 200 kV and point resolution of 0.25 nm, therein the carbon layer fringes were captured by a CCD camera with a pixel resolution of 2688 by 2672 at an optimised magnification of 470,000 times (0.016 nm/pixel). Fig. 4 shows this TEM image processing procedures. Firstly, soot aggregates with some primary particles jutting out from the lacy carbon film were identified by a brief browsing to the lacy TEM grid sample at a low magnification. This approach is vital to capture clear carbon fringe information inside soot primary particles with no background interference from the grid film. In the selected soot aggregate (Fig. 4b), a primary particle that does not overlap with others is then imaged for high-resolution imaging. As shown in Fig. 4c, the soot internal pattern is unveiled in a form of carbon layer fringes with variations in physical extent, degree of curvature and the spacing gaps between the layers. These geometric features of carbon fringes directly reflect the status of soot graphitisation, and thus provide key information on the status of soot formation/oxidation and reactivity [43] through the quantification of fringe length, tortuosity and fringe separation distance [51,52]. This processing is shown in Fig. 4d–h. It was noted that very small fringes that are smaller than the size of aromatic rings (e.g. 0.24 nm [53]) were considered as artifacts and thus removed [39,40,43]. Although manual selection of fringe pairs is required to determine the distance between two neighbouring fringes (Fig. 4g), the fringe length and tortuosity were processed automatically [43]. For each high-resolution TEM sample, a total of 10 images were acquired from various on-grid locations, which resulted in over 8000 carbon fringes and more than 1000 fringe pairs.

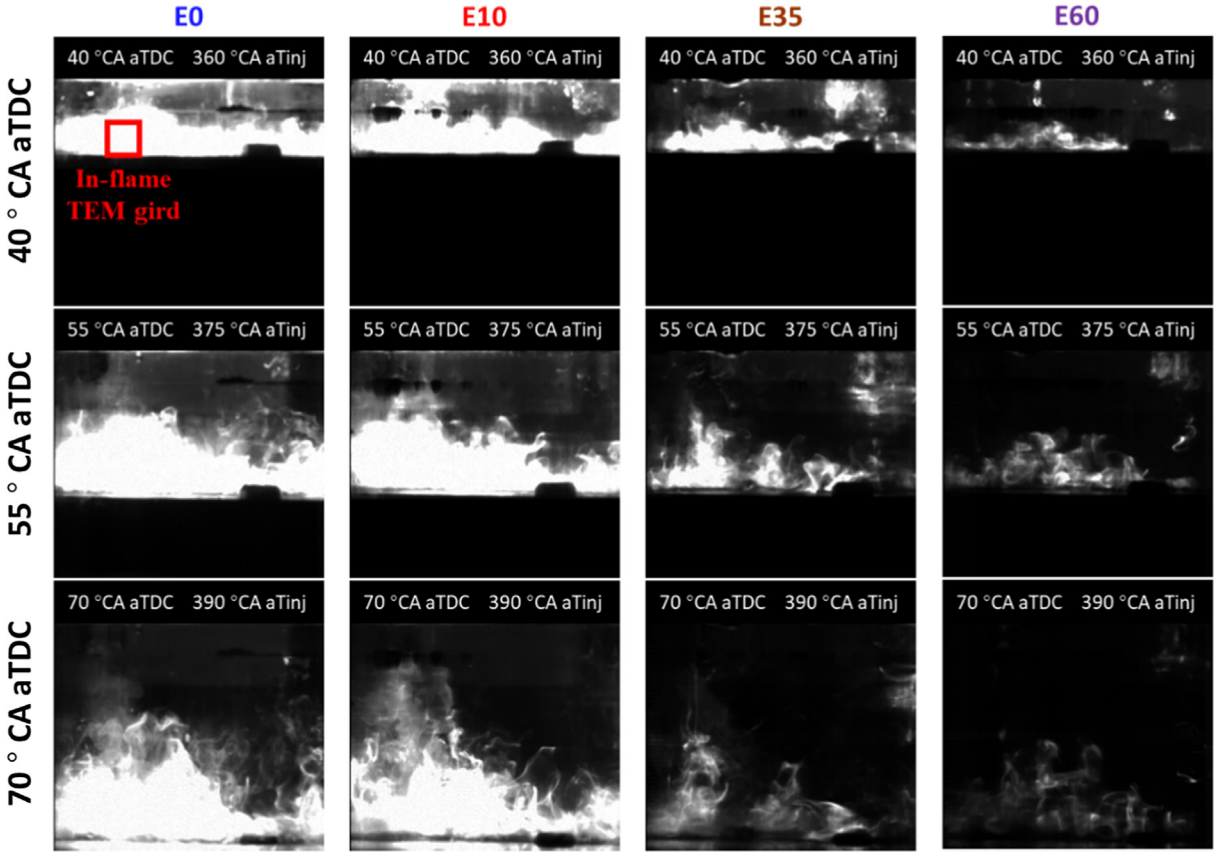

Fig. 6. Soot luminosity signals captured through the cylinder liner window at various crank angle locations and ethanol blending ratios.

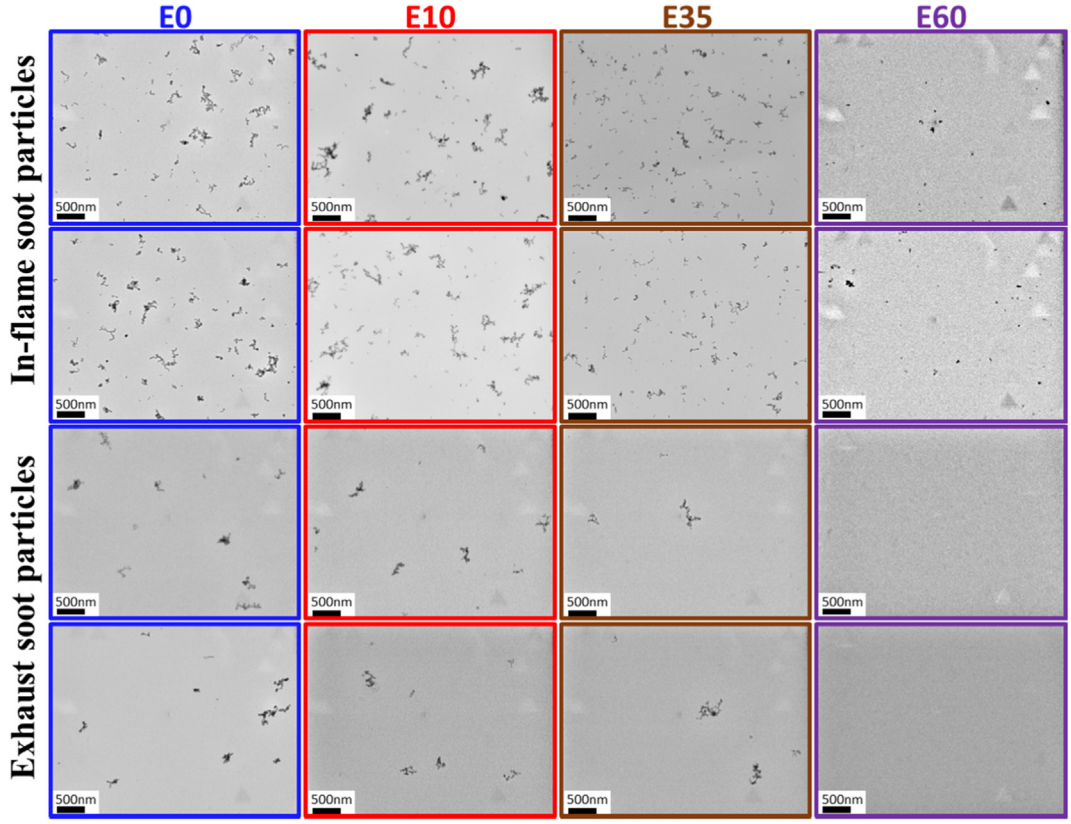

Fig. 7. Selected standard TEM images for in-flame (top two rows) and exhaust (bottom two rows) soot particles with 30,000 magnification setting. The scale bar of 500 nm is shown on each image.

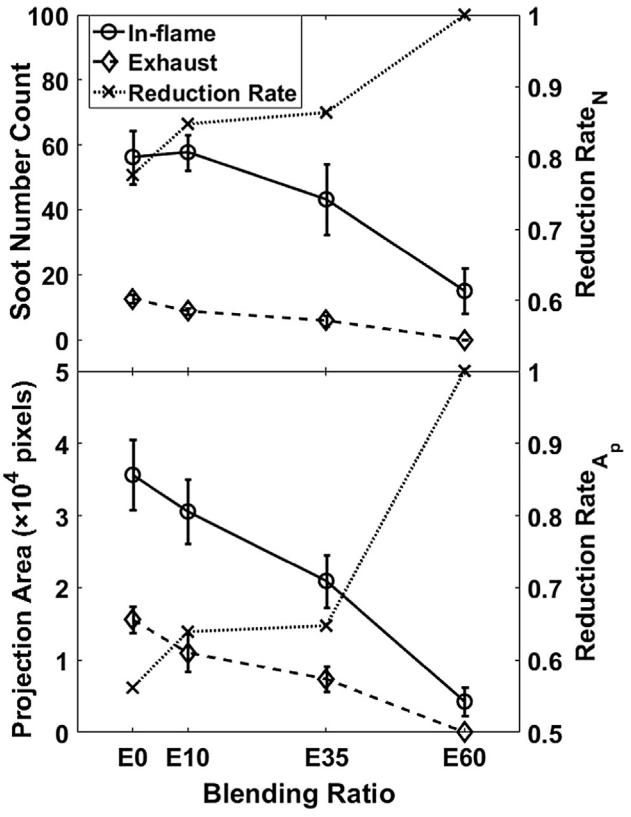

Fig. 8. Soot number counts, projection area and their reduction rate for various ethanol blending ratios.

3. Results and discussion

3.1. In-cylinder pressure and high-speed soot luminosity images

The in-cylinder pressure and apparent heat release rate (aHRR) for a total of 8 soot sampling experiment sets are shown in Fig. 5. Each of standard and lacy TEM grid experiments was repeated for various ethanol blending ratios while the grids were loaded in both in-flame and exhaust samplers. As the stoichiometric charge was made by injecting more fuel at higher ethanol blending ratio, the spark timing was adjusted until the in-cylinder pressure and aHRR traces are well matched for various ethanol blending ratios, which effectively isolate the fuel effect on soot formation and oxidation from combustion conditions. This was done through a trial-and-error approach such that the ensemble-averaged in-cylinder pressure trace was compared to other runs and if it was not consistent with others, the TEM grids were disposed.

While the in-cylinder pressure and aHRR traces were well matched regardless of the ethanol blending ratio, the soot luminosity images shown in Fig. 6 indicates very different sooting levels. Fig. 6 shows soot luminosity images obtained through a cylinder liner window (i.e. side-view) with the piston moving downwards during the expansion stroke from 40 to 70 crank angle degree after the top dead centre (°CA aTDC) or 360 to 390 °CA after the injection (°CA aT_{inj}). On the right side of each image, a soot sampling probe (unused in the present study) is seen as a shadow caused by the strong soot luminosity signals. The used in-flame soot sampling probe is within the soot luminosity region as illustrated by a red square at the image top-left.

From the soot luminosity images, it is clear that the early 320 °CA bTDC injection caused wall wetting on the piston top surface, which induced significant pool fire. Also, the pool fire is found more significant on the left side in the soot luminosity images as the fuel injection was directed from right to left. This was where the in-flame soot

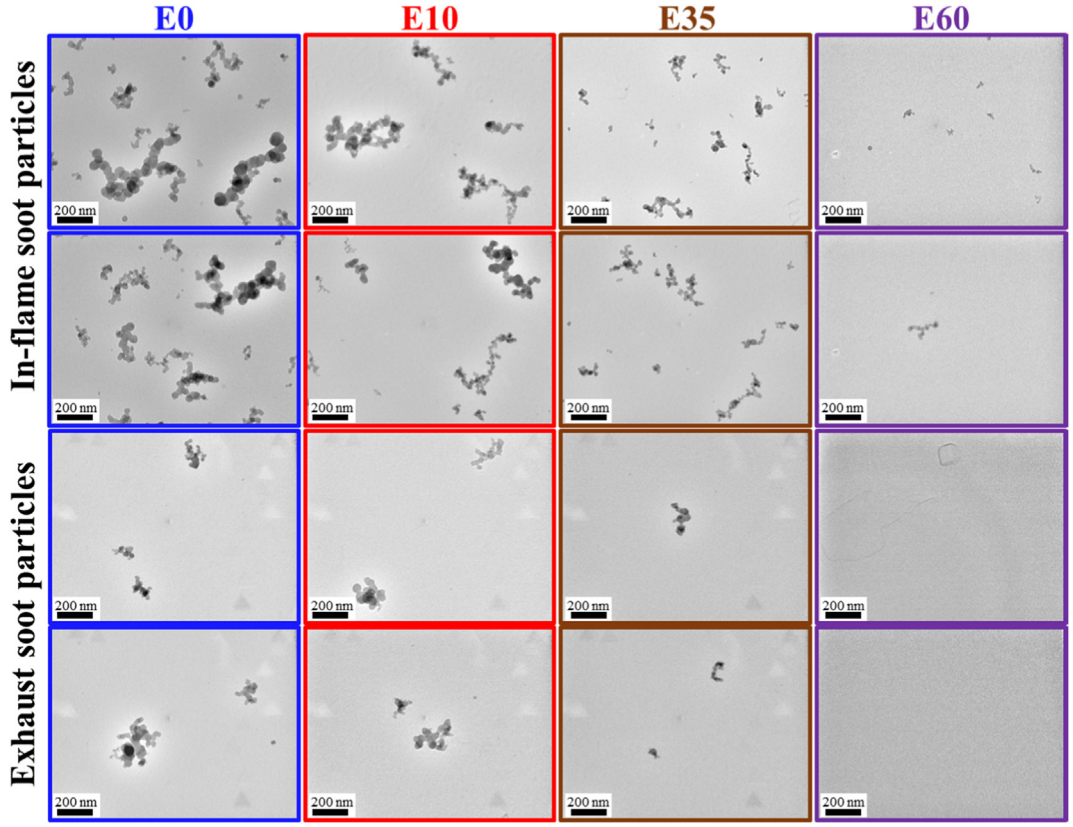

Fig. 9. Sampled in-flame (top two rows) and exhaust (bottom two rows) soot particles in the standard TEM images with 100,000 magnification setting. The scale bar of 200 nm is shown on each image.

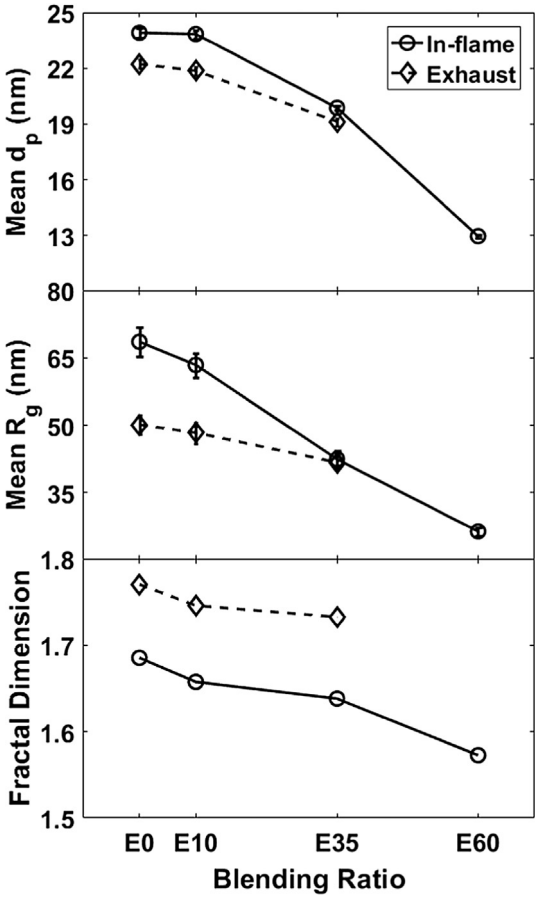

Fig. 10. Mean values of soot primary particle diameter (top), aggregates radius of gyration (middle) and fractal dimension (bottom) for various ethanol blending ratios. The error range is estimated with 95% confidence.

sampling probe is located in the present study and thus suitable for soot structure discussion depending on the ethanol blending ratio.

The soot luminosity images suggest that the pool fire was the most intensive at E0 with the TEM grid being exposed to the flames for a long period of time. Interesting, the soot luminosity signals appear very similar between E0 and E10 despite 10% of the petrol being substituted by oxygenated and thus low-sooting ethanol. However, at E35, the soot luminosity is significantly reduced with the pool fire height being only about a half of that for E0 and E10. The decreasing trend continues for E60 with little amount of soot luminosity signals indicating minimal exposure of the TEM grid to sooting flames. The lower soot propensity was expected due to the use of oxygenated ethanol, which helps reduce soot formation and enhance soot oxidation [20]. It should be noted that the injection duration was increased from 2.40 to 3.08 ms as the ethanol blending ratio was increased from 0 to 60%. This means higher wall wetting was expected as the fuel impinged on the piston top surface for a longer period of time. Also, ethanol has higher density and viscosity (see Table 2), which would increase wall wetting. However, the soot luminosity images clearly show lower soot for higher ethanol ratios, suggesting that the oxygenated ethanol caused lower sooting conditions despite possibly higher wall wetting.

3.2. Soot aggregate number counts and projection area

Fig. 7 shows some selected standard TEM images taken at low magnification (30k) for various ethanol blending ratios. The top two rows show in-flame soot particles/aggregates and the corresponding exhaust soot particles of the same firing cycles are shown at the bottom two rows. From visual inspection, a clear trend is observed that, for a fixed ethanol blending ratio, the exhaust soot particles are much lower in the number counts and simpler in their structure than the in-flame particles, both of which evidence significant soot oxidation occurring inside the cylinder. It is also seen that the in-flame soot particles are larger at lower ethanol blending ratios of E0 and E10 compared to E35 exhibiting smaller soot particles. At E60, the sampled soot particles are rare and they are very small and compact in structure. The overall decreasing soot trend is also found in the exhaust soot particles with a gradual decrease in both the overall soot area and the number counts with increasing ethanol blending ratio. At E60, no soot particles were sampled from the exhaust stream, which is consistent with very low sooting level of the in-flame sample. The decreasing exhaust soot in both the number and mass due to higher ethanol blending ratio was previously reported [12,26], with Fig. 7 providing new information that the in-flame soot was also lower at higher ethanol blending ratio and there was a dramatic reduction in soot number counts and amounts between the flame and exhaust gas.

Fig. 8 shows the plot of soot number counts and projection area based on all 10 TEM images for each ethanol blending ratio. The error bar with 95% confidence is shown in each blending ratio. In addition to the in-flame and exhaust soot number counts and projection area, their reduction rate due to soot oxidation was also calculated as shown in Fig. 8. This statistical analysis shows a clear trend that both number counts and projection area of the exhaust soot particles are significantly lower than those of the in-flame soot, indicating a high rate of soot oxidation occurring inside the cylinder. With increasing ethanol blending ratio, both the number counts and project area of in-flame and exhaust soot particles decline almost linearly. However, it is noticeable that both the number counts and project area reduction for the in-flame soot particles are steeper than that of the exhaust soot particles. That is, the soot decrease due to oxygenated ethanol is much more effective within the flame as the fuel molecular structure directly impacted the soot formation.

An interesting non-monotonic trend is also observed from Fig. 8. For instance, the in-flame soot counts of E0 and E10 are almost identical while the soot projection area is lower for E10. This suggests more active particle-to-particle agglomeration for E0 with no significant suppressing effect of oxygenated ethanol on soot formation. Such finding was not made in previous studies focused on exhaust soot particles only. The soot reduction rate also shows a non-monotonic trend. Both the number counts and projection area reduction between the in-flame and exhaust soot is higher for E10 than those of E0. A similar reduction rate is observed for E10 and E35 until significantly higher reduction rate is measured for E60. This indicates the soot oxidation is enhanced at a similar magnitude for low to medium ethanol blending ratios, and there is a threshold in the ethanol blending ratio that can completely eliminates all the in-flame soot particles, which was 60% in the tested conditions. Once again, this finding could only be made due to the simultaneous investigation of in-flame and exhaust soot particles.

3.3. Size and structure of soot primary particles and aggregates

The TEM images previously shown in Fig. 7 were useful to discuss the overall sooting level; however, its low resolution made it impossible to reduce the data for soot size distribution and structure analysis. Fig. 9 shows example TEM images of the same grid as in Fig. 7 but at a higher magnification setting of 100,000 times. From these higher magnification images, variations in soot particle size and structure are clearly seen. For example, it is observed that the in-flame soot particles are mostly soot aggregates of many soot primary particles with complex fractal structures that also vary aggregate by aggregate. When the soot aggregates are sampled from the exhaust gas, however, the aggregates become much more compact and simple in structure. This structural change from the in-flame soot to exhaust particles was previously reported [48], which proposed the fragmentation of large aggregates and

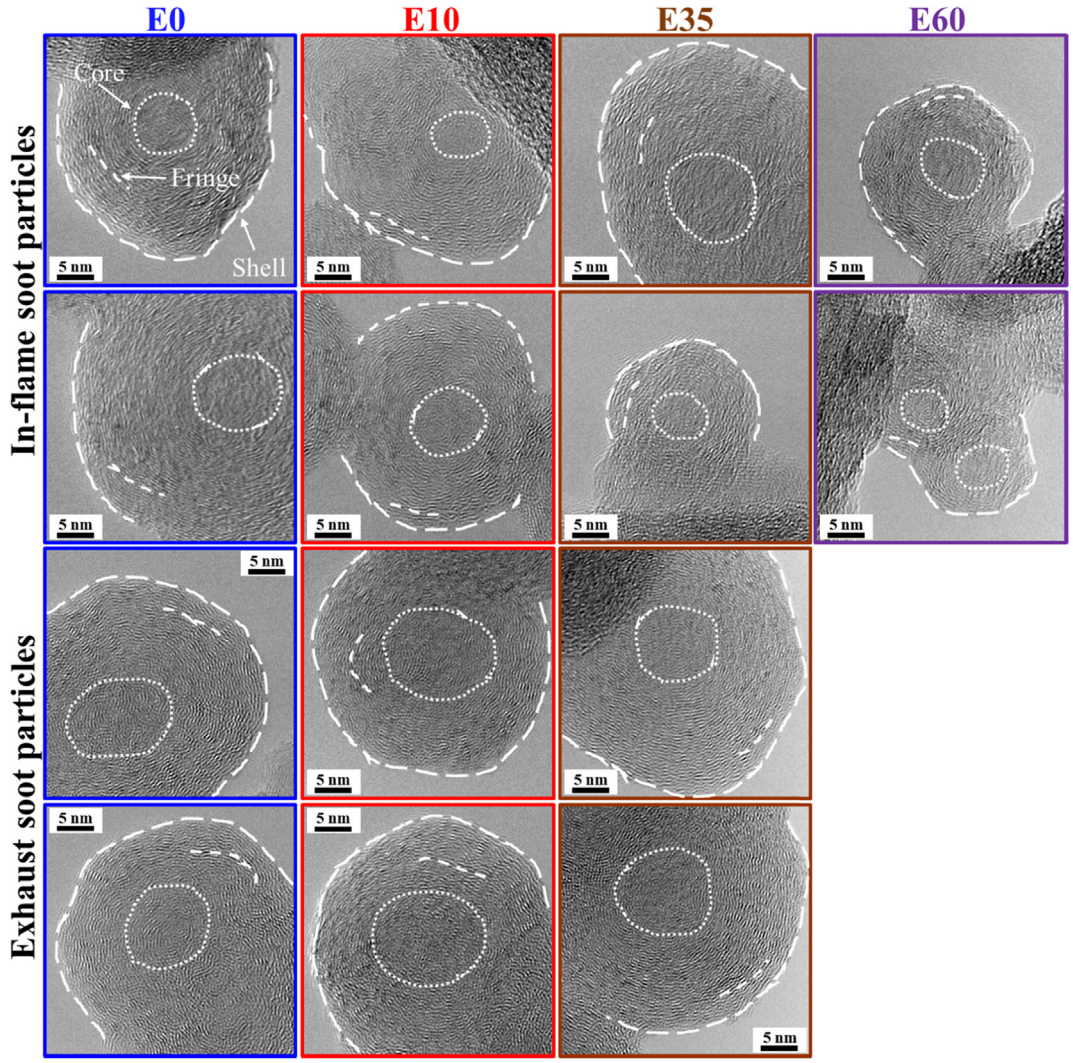

Fig. 11. Sampled in-flame (top two rows) and exhaust (bottom two rows) soot particles in lacy 470k TEM images.

the complete disappearance of small aggregates as the in-cylinder soot oxidation mechanism.

The increased ethanol ratio significantly influences the soot aggregate structure. Fig. 9 shows that, with increasing ethanol blending ratio, the in-flame soot aggregates become smaller in size and simpler in structure. Interestingly, both E0 and E10 show very large soot aggregates of a couple of hundreds nanometre. However, E35 shows mostly small aggregates and E60 shows the most compact aggregate structures. The exhaust soot particles, regardless of the ethanol blending ratio, exhibit compact aggregate structures with the size reduction occurring for higher ethanol blending ratio.

From many TEM images similar to Fig. 9, over 100 soot aggregates and more than 1000 soot primary particles were processed for each sample, which enabled the statistical analysis of primary particle size (diameter, d_p), aggregate size (radius of gyration, R_g) and fractal dimension (D_f). The results are shown in Fig. 10. As expected, it is observed that both d_p and R_g for the exhaust soot are lower than those for the in-flame soot particles due to soot oxidation. This, together with higher D_f, suggests that the in-cylinder soot oxidation occurred though the concurrent reduction of soot primary particles and the breakdown of large soot aggregates from the outer branches. The result is a less stretched, compact soot aggregate composed of smaller primary particles in the exhaust gas, compared to a long-stretched in-flame soot aggregate comprising larger primary particles.

With increasing ethanol blending ratio, both in-flame and exhaust soot aggregates/particles show a decreasing trend for d_p, R_g and D_f. The original cause of this trend is the formation of soot particles that are smaller and simpler in structure. Specifically, all of the soot formation process including the soot precursor formation, nucleation, surface growth and subsequent aggregation would be suppressed due to the oxygen in fuel [54–56]. Detailed mechanism of soot suppression in alcohol fuel is explained that carbon atoms will be absent from the elementary reactions to combine with other kinds if they are initially bonded with an oxygen atom in the fuel molecule [57]. Moreover, as the ethanol blending ratio increases, the aromatic content decreases, which also contributes to lower d_p and R_g as previously reported [58,59]. As shown in Fig. 6, it is also lower soot residence time that would suppress the soot formation in terms of the surface growth and aggregate coagulation [60]. Not only is d_p and R_g lower but also D_f because the in-flame soot has more stretched chain-like structures that are easier to be broken.

Consistent with more significant reduction in in-flame soot number counts and projection area (Fig. 8), the results in Fig. 10 also shows higher decrease of d_p and R_g for the in-flame soot than those of the exhaust soot. The in-flame reduction of d_p and R_g becomes so significant that, at E35, the in-flame and exhaust soot show almost the same d_p and R_g. This should be interpreted as significantly low soot formation within the flame, which did not require high oxidation rate to cause low exhaust soot. The trend continues such that at E60, no exhaust soot particles are sampled.

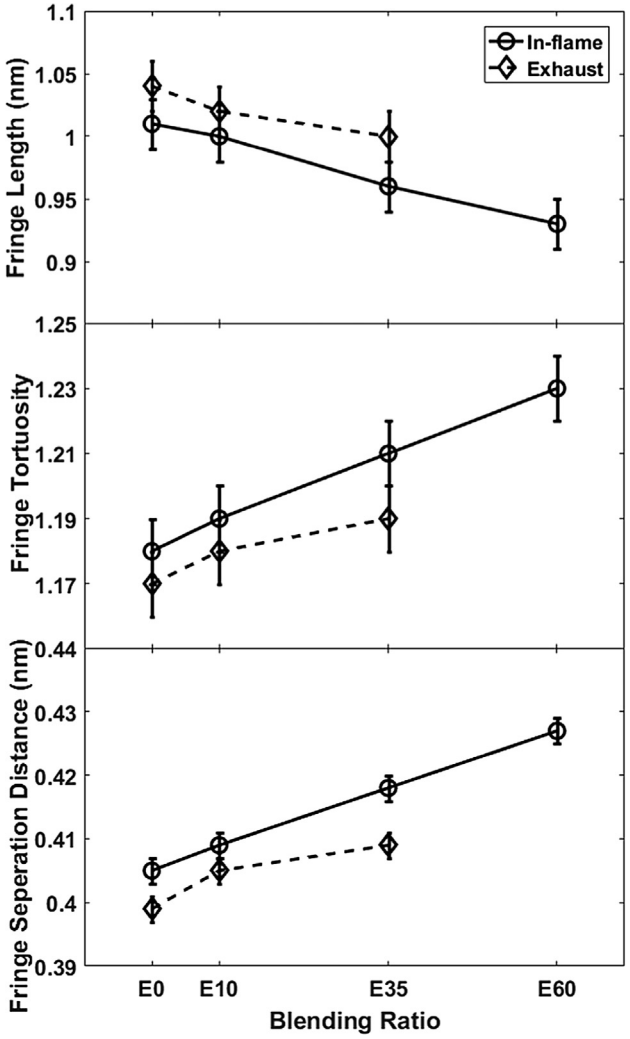

Fig. 12. Mean values of fringe length (top), fringe tortuosity (middle) and fringe separation distance (bottom) for all tested fuels. The error ranges are estimated with 95% confidence.

3.4. Soot internal structures

Fig. 11 shows selected high-resolution TEM images of the sampled in-flame and exhaust soot particles using lacy grids. The high magnification setting of 470,000 times enabled the visualisation of carbon layer fringes and thus the discussion of soot internal structures. The scale bar of 5 nm is shown on each image. Through visual inspection, similar patterns of both in-flame and exhaust soot particles are shown which does not vary with the ethanol blending ratio, i.e. a soot particle is composed of short and long stacked graphene layers, namely, "fringes", with shorter graphene layers of amorphous pattern forming the inner core region and longer and more ordered fringes forming the outer shell. This overall structure is highlighted by the white dashed lines. These images were processed so that three sub-nanoscale parameters of fringe length, fringe tortuosity and fringe separation distance are estimated. The results are shown in Fig. 12 for various ethanol blending ratios with the 95% confidence error bars. The three fringe parameters show a consistent trend that, compared to the in-flame soot, the exhaust soot particles are composed of carbon layers with longer fringe length, lower tortuosity and smaller fringe gap due to oxidation. With increasing ethanol blending ratio, there is a monotonic trend of decreasing fringe length, increasing tortuosity and increase fringe separation, which indicates less graphitised particle structure, and thus more reactive and more premature soot formation due to oxygen in fuel. This is similar to the soot particles of biodiesel, another oxygenated fuel [40]. These internal structures of in-flame soot particles directly impact the exhaust soot with exactly the same trend observed for all three parameters.

4. Conclusions

The effects of ethanol blending ratio on the in-flame and exhaust soot particles have been investigated in a single-cylinder optical SIDI engine. Soot particles of a conventional petrol fuel and various ethanol blends were collected directly from the flames inside the cylinder using a thermophoretic sampling technique, which were compared to the sampled exhaust soot particles. The sampled soot particles onto TEM grids were imaged for detailed analysis of soot number counts, projection area, primary particle diameter, and radius of gyration of soot aggregates as well as fractal dimension. Using lacy TEM grids, sub-nanoscale carbon layer fringe parameters were also analysed for soot internal structures. This experimental study has achieved a few unique findings that were not possible based solely on exhaust soot analysis as follows:

- Significant reduction in number counts and projection area is found between the in-flame and exhaust soot at any fixed ethanol blending ratio. The soot aggregates and primary particles in the exhaust sample are smaller in size and show less stretched structures due to significant soot oxidation occurring inside the cylinder. This is also evident in the soot internal structure with longer and straighter fringes with narrower separation for the exhaust sample.
- With increasing ethanol blending ratio, the soot number counts and project area decrease for both in-flame and exhaust soot particles. The soot aggregates and primary particles become smaller with more stretched aggregates structures. This indicates significant suppression of soot formation at higher ethanol blending ratios. The shorter, more curved, and separated fringe patterns also indicate more reactive soot particles formation within the flame for higher ethanol blending ratio, which results in exhaust soot particles with more reactive structures.
- The effect of ethanol blending on soot was more significant in in-flame particles than exhaust particles. The reduction of number counts, project area as well as the size of primary particles and aggregates is much higher for the in-flame soot than that of the exhaust soot, indicating the suppressed soot formation within the flame plays a major role in significantly reduced engine-out soot for higher ethanol blending ratios. The soot oxidation following the initial formation could increase with increasing ethanol blending ratio; however, it is the lower soot formation that makes more dominant effect on the final soot product in the exhaust stream.

Acknowledgments

Experiments were performed at the UNSW Engine Research Laboratory, Sydney, Australia. Support for this research was provided by the SJTU-UNSW Collaborative Research Fund. We also appreciate the China Scholarship Council (CSC) for the visiting fellowship.

References

[1] Whitaker P, Kapus P, Ogris M, Hollerer P. Measures to reduce particulate emissions from gasoline DI engines. SAE Int J Engines 2011;4(1):1498–512.
[2] Bhandarkar S. Vehicular pollution, their effect on human health and mitigation measures. Veh Eng 2013;1(2):3340.
[3] European Commission. Commission Regulation (EC) No. 692/2008 of 18 July 2008. Off J Eur Union 2008.
[4] Chan TW, Meloche E, Kubsh J, Rosenblatt D, Brezny R, Rideout G. Evaluation of a gasoline particulate filter to reduce particle emissions from a gasoline direct injection vehicle. SAE Int J Fuels Lubr 2012;5(3):1277–90.
[5] Pischinger S. Current and future challenges for automotive catalysis: engine technology trends and their impact. Top Catal 2016;59(10–12):834–44.

[6] Hoffmann G, Befrui B, Berndorfer A, Piock WF, Varble DL. Fuel system pressure increase for enhanced performance of GDi multi-hole injection systems. SAE Int J Engines 2014;7(1):519–27.
[7] Piock WF, Befrui B, Berndorfer A, Hoffmann G. Fuel pressure and charge motion effects on GDi engine particulate emissions. SAE Int J Engines 2015;8(2):464–73.
[8] Bielaczyc P, Woodburn J, Gandyk M, Szczotka A. Ethanol as an automotive fuel – a review. Combust Engines 2016;55(3):39–45.
[9] Oliveria MED, Vaughan BE, Rykiel Jr. E. Ethanol as fuel: energy, carbon dioxide balances, and ecological footprint. Bioscience 2005;55(7):593–602.
[10] Hansen AC, Zhang Q, Lyne PWL. Ethanol–diesel fuel blends – a review. Bioresour Technol 2005;96(3):277–85.
[11] Demirbas A. Political, economic and environmental impacts of biofuels: a review. Appl Energy 2009;86:S108–17.
[12] Fatouraie M, Wooldridge M, Wooldridge S. In-cylinder particulate matter and spray imaging of ethanol/gasoline blends in a direct injection spark ignition engine. SAE Int J Fuels Lubr 2013;6(1):1–10.
[13] Szybist JP, Youngquist AD, Barone TL, Storey JM, Moore WR, Foster M, et al. Ethanol blends and engine operating strategy effects on light-duty spark-ignition engine particle emissions. Energy Fuels 2011;25(11):4977–85.
[14] Karavalakis G, Short D, Vu D, Russell RL, Asa-Awuku A, Jung H, et al. The impact of ethanol and iso-butanol blends on gaseous and particulate emissions from two passenger cars equipped with spray-guided and wall-guided direct injection SI (spark ignition) engines. Energy 2015;82:168–79.
[15] Karavalakis G, Short D, Vu D, Villela M, Russell R, Jung H, et al. Regulated emissions, air toxics, and particle emissions from SI-DI light-duty vehicles operating on different iso-butanol and ethanol blends. SAE Int J Fuels Lubr 2014;7(1):183–99.
[16] Wang C, Xu H, Herreros JM, Wang J, Cracknell R. Impact of fuel and injection system on particle emissions from a GDI engine. Appl Energy 2014;132:178–91.
[17] Chan TW. The impact of isobutanol and ethanol on gasoline fuel properties and black carbon emissions from two light-duty gasoline vehicles. SAE paper 2015-01-1076. 2015.
[18] Cho J, Si W, Jang W, Jin D, Myung C-L, Park S. Impact of intermediate ethanol blends on particulate matter emission from a spark ignition direct injection (SIDI) engine. Appl Energy 2015;160:592–602.
[19] Graves BM, Koch CR, Olfert JS. Morphology and volatility of particulate matter emitted from a gasoline direct injection engine fuelled on gasoline and ethanol blends. J Aerosol Sci 2017;105:166–78.
[20] Maricq MM. Soot formation in ethanol/gasoline fuel blend diffusion flames. Combust Flame 2012;159(1):170–80.
[21] Lemaire R, Therssen E, Desgroux P. Effect of ethanol addition in gasoline and gasoline–surrogate on soot formation in turbulent spray flames. Fuel 2010;89(12):3952–9.
[22] Chen L, Stone R, Richardson D. A study of mixture preparation and PM emissions using a direct injection engine fuelled with stoichiometric gasoline/ethanol blends. Fuel 2012;96:120–30.
[23] Bielaczyc P, Woodburn J, Klimkiewicz D, Pajdowski P, Szczotka A. An examination of the effect of ethanol–gasoline blends' physicochemical properties on emissions from a light-duty spark ignition engine. Fuel Process Technol 2013;107:50–63.
[24] Chen L, Stone R. Measurement of enthalpies of vaporization of isooctane and ethanol blends and their effects on PM emissions from a GDI engine. Energy Fuels 2011;25(3):1254–9.
[25] Karavalakis G, Short D, Vu D, Russell R, Asa-Awuku A, Durbin T. A complete assessment of the emissions performance of ethanol blends and iso-butanol blends from a fleet of nine PFI and GDI vehicles. SAE Int J Fuels Lubr 2015;8(2015-01-0957):374–95.
[26] Lee PI, Feng X, Lai MC. Gasoline and E85 combustion visualization and particulate matter emission in a production SIDI engine with optical access. ASME 2013 internal combustion engine division fall technical conference, Dearborn, Michigan, USA. 2013.
[27] Storch M, Koegl M, Altenhoff M, Will S, Zigan L. Investigation of soot formation of spark-ignited ethanol-blended gasoline sprays with single- and multi-component base fuels. Appl Energy 2016;181:278–87.
[28] Luo Y, Zhu L, Fang J, Zhuang Z, Guan C, Xia C, et al. Size distribution, chemical composition and oxidation reactivity of particulate matter from gasoline direct injection (GDI) engine fueled with ethanol-gasoline fuel. Appl Therm Eng 2015;89:647–55.
[29] Wang Y, Zheng R, Qin Y, Peng J, Li M, Lei J, et al. The impact of fuel compositions on the particulate emissions of direct injection gasoline engine. Fuel 2016;166:543–52.
[30] Karavalakis G, Short D, Vu D, Villela M, Asa-Awuku A, Durbin TD. Evaluating the regulated emissions, air toxics, ultrafine particles, and black carbon from SI-PFI and SI-DI vehicles operating on different ethanol and iso-butanol blends. Fuel 2014;128:410–21.
[31] Maricq MM, Szente JJ, Jahr K. The impact of ethanol fuel blends on PM emissions from a light-duty GDI vehicle. Aerosol Sci Technol 2012;46(5):576–83.
[32] Short D, Vu D, Durbin TD, Karavalakis G, Asa-Awuku A. Particle speciation of emissions from iso-butanol and ethanol blended gasoline in light-duty vehicles. J Aerosol Sci 2015;84:39–52.
[33] Storch M, Zigan L, Wensing M, Will S. Systematic investigation of the influence of ethanol blending on sooting combustion in DISI engines using high-speed imaging and LII. SAE paper 2014-01-2617. 2014.
[34] Wang C, Xu H, Herreros JM, Lattimore T, Shuai S. Fuel effect on particulate matter composition and soot oxidation in a direct-injection spark ignition (DISI) engine. Energy Fuels 2014;28(3):2003–12.
[35] Lee KO, Seong H, Sakai S, Hageman M, Rothamer D. Detailed morphological properties of nanoparticles from gasoline direct injection engine combustion of ethanol blends. SAE paper 2013-24-0185. 2013.
[36] Seong H, Lee K, Choi S. Effects of engine operating parameters on morphology of particulates from a gasoline direct injection (GDI) engine. SAE paper 2013-01-2574. 2013.
[37] Barone TL, Storey JME, Youngquist AD, Szybist JP. An analysis of direct-injection spark-ignition (DISI) soot morphology. Atmos Environ 2012;49:268–74.
[38] Zhang R, Kook S. Structural evolution of soot particles during diesel combustion in a single-cylinder light-duty engine. Combust Flame 2015;162(6):2720–8.
[39] Zhang Y, Kim D, Rao L, Zhang R, Kook S, Kim KS, et al. The soot particle formation process inside the piston bowl of a small-bore diesel engine. Combust Flame 2017;185:278–91.
[40] Zhang Y, Zhang R, Rao L, Kim D, Kook S. The influence of a large methyl ester on in-flame soot particle structures in a small-bore diesel engine. Fuel 2017;194:423–35.
[41] Gaddam CK, Vander Wal RL. Physical and chemical characterization of SIDI engine particulates. Combust Flame 2013;160(11):2517–28.
[42] Wu Z, Song C, Lv G, Pan S, Li H. Morphology, fractal dimension, size and nanostructure of exhaust particles from a spark-ignition direct-injection engine operating at different air–fuel ratios. Fuel 2016;185:709–17.
[43] Zhang Y, Zhang R, Kook S. Nanostructure analysis of in-flame soot particles under the influence of jet-jet interactions in a light-duty diesel engine. SAE Int J Engines 2015;8(5):2213–26.
[44] Li Z, Song C, Song J, Lv G, Dong S, Zhao Z. Evolution of the nanostructure, fractal dimension and size of in-cylinder soot during diesel combustion process. Combust Flame 2011;158(8):1624–30.
[45] Chan QN, Bao Y, Kook S. Effects of injection pressure on the structural transformation of flash-boiling sprays of gasoline and ethanol in a spark-ignition direct-injection (SIDI) engine. Fuel 2014;130:228–40.
[46] Clark LG, Kook S, Chan QN, Hawkes ER. Multiple injection strategy investigation for well-mixed operation in an optical wall-guided spark-ignition direct-injection (WG-SIDI) engine through flame shape analysis. SAE paper 2016-01-2162. 2016.
[47] Clark LG, Kook S, Chan QN, Hawkes ER. Influence of injection timing for split-injection strategies on well-mixed high-load combustion performance in an optically accessible spark-ignition direct-injection (SIDI) engine. SAE paper 2017-01-0657. 2017.
[48] Kim D, Zhang Y, Clark L, Kook S, Gao Y. In-flame soot sampling and morphology analysis in an optical spark-ignition direct-injection (SIDI) Engine. SAE paper 2018-01-1418. 2018.
[49] VIVA Energy Australia Pty Ltd. Shell unleaded petrol 95. 2016 [accessed 1 February 2017].
[50] Kook S, Zhang R, Chan QN, Aizawa T, Kondo K, Pickett LM, et al. Automated detection of primary particles from transmission electron microscope (TEM) images of soot aggregates in diesel engine environments. SAE Int J Engines 2015;9(1):279–96.
[51] Sakai M, Iguma H, Kondo K, Aizawa T. Nanostructure analysis of primary soot particles directly sampled in diesel spray flame via HRTEM. SAE paper 2012-01-1722. 2012.
[52] Yehliu K, Vander Wal RL, Boehman AL. Development of an HRTEM image analysis method to quantify carbon nanostructure. Combust Flame 2011;158(9):1837–51.
[53] Shim H-S, Hurt RH, Yang NYC. A methodology for analysis of 0 0 2 lattice fringe images and its application to combustion-derived carbons. Carbon 2000;38(1):29–45.
[54] Herbinet O, Pitz WJ, Westbrook CK. Detailed chemical kinetic oxidation mechanism for a biodiesel surrogate. Combust Flame 2008;154(3):507–28.
[55] Pepiot-Desjardins P, Pitsch H, Malhotra R, Kirby SR, Boehman AL. Structural group analysis for soot reduction tendency of oxygenated fuels. Combust Flame 2008;154(1):191–205.
[56] Buchholz BA, Mueller CJ, Upatnieks A, Martin GC, Pitz WJ, Westbrook CK. Using carbon-14 isotope tracing to investigate molecular structure effects of the oxygenate dibutyl maleate on soot emissions from a DI diesel engine. SAE paper 2004-01-1849. 2004.
[57] Westbrook CK, Pitz WJ, Curran HJ. Chemical kinetic modeling study of the effects of oxygenated hydrocarbons on soot emissions from diesel engines. J Phys Chem A 2006;110:6912–22.
[58] Wei J, Song C, Lv G, Song J, Wang L, Pang H. A comparative study of the physical properties of in-cylinder soot generated from the combustion of n-heptane and toluene/n-heptane in a diesel engine. Proc Combust Inst 2015;35(2):1939–46.
[59] Okabe K, Sakai M, Mizutani Y, Aizawa T. Aromatic additive effect on soot formation and oxidation in Fischer-Tropsch diesel (FTD) spray flame-morphology and nanostructure analysis of in-flame soot particles via HRTEM. SAE Int J Fuels Lubr 2013;6(3):807–16.
[60] Ito H, Fujita O, Ito K. Agglomeration of soot particles in diffusion flames under microgravity. Combust Flame 1994;99(2):363–70.